Journal of ELECTRONIC MATERIALS, Vol. 46, No. 7, 2017
DOI: 10.1007/s11664-017-5463-3

Low Temperature Synthesis and Properties of $BiFeO_3$

ASAD FEROZE,[1,2] MUHAMMAD IDREES,[1,6] DEOK-KEE KIM,[2]
MUHAMMAD NADEEM,[3] SAADAT A. SIDDIQI,[4] SALEEM F. SHAUKAT,[1]
MUHAMMAD ATIF,[5] and MUHAMMAD SIDDIQUE[3]

1.—Department of Physics, COMSATS Institute of Information and Technology, Defense Road, Off Raiwind Road, Lahore 54600, Pakistan. 2.—Department of Electrical Engineering, Sejong University, Seoul 143-747, Republic of Korea. 3.—EMMG, Physics Division, PINSTECH, Nilore, Islamabad, Pakistan. 4.—IRCBM, COMSATS Institute of Information and Technology, Defense Road, Off Raiwind Road, Lahore 54600, Pakistan. 5.—Functional Materials Lab, Department of Physics, Air University, PAF Complex, E-9, Islamabad, Pakistan. 6.—e-mail: asadbutt5@yahoo.com

Extensive efforts have been made to synthesize single phase and stoichiometric $BiFeO_3$. Some modified techniques have been tried in synthesizing $BiFeO_3$ as compared with the conventionally used co-precipitation method. Thermogravimetric Analysis/Differential Scanning Calorimetry and x-ray diffraction experiments were used exclusively to explore the effects of heat treatment temperature and time on crystallographic behavior of the prepared $BiFeO_3$ powder. Field emission scanning electron microscopy was used to explore the microstructure of the synthesized $BiFeO_3$. The appearance of different magnetic phases in ^{57}Fe Mössbauer spectra and field dependent magnetization was confirmed on the basis of particle size distribution. In this research, an easy, low cost and high-yield method for the low temperature single phase and stoichiometric synthesis of $BiFeO_3$ has been suggested.

Key words: Multiferroic, chemical synthesis, vacancy formation, ^{57}Fe Mössbauer spectroscopy

INTRODUCTION

Multiferroics are materials that exhibit more than one primary ferroic or anti-ferroic properties in a single phase. These materials in ferroic properties are also coupled with each other.[1] Among multiferroics, the materials exhibiting coupled ferroelectric (anti-ferroelectric) and ferromagnetic (anti-ferromagnetic) behavior in single phase are called magneto-electric materials. The coupling between electrically and magnetically ordered parameters opens a new window to improve performance and efficiency of the devices used in data storage, communications, spintronics, random access memories (RAMs), and optoelectronics.[2–7] For example, use of magneto-electric materials in data storage does not need high applied magnetic field for data encoding. There are very few materials existing in nature or synthesized in the laboratory, like $KNiPO_4$, Sm_2CuO_4, Gd_2CuO_4, $LiCoPO_4$, $ReMn_2O_5$, $ReMnO_3$ (Re is a rare earth metal), NiB_7O_{12}, $Tb_2(MoO_4)_3$, $BiMnO_3$, boracites, hexaferrites, and $BaMnF_4$, that show both ferroic properties at or above room temperature.

The commercial use of magneto-electric materials is limited due to poor coupling between electric and magnetic order parameters at room temperature. Among known magneto-electric materials, $BiFeO_3$ is the strongest candidate for commercial applications due to its unique and strong coupling between electric and magnetic order parameters at room temperature. However, hard and complex single phase synthesis and lack of understanding of fundamental $BiFeO_3$ properties restrict commercial use. Because of the evaporation of oxygen, bismuth and the existence of Fe^{+2}, Fe^{+3} results in impurity phases and degrades the intrinsic unique properties of $BiFeO_3$. Use of advanced low temperature synthesis techniques is a better approach to avoid bismuth and oxygen evaporation, which makes it suitable for single phase synthesis of $BiFeO_3$. A

(Received August 12, 2016; accepted March 17, 2017;

comparison of different $BiFeO_3$ synthesis techniques in practice is described in Table I. It is emphasized in Table I that the use of these methods requires the hard control of synthesis parameters, such as the liquid medium, during milling, milling time, milling speed, heat treatment time, pressure, PH, and various temperature treatment steps such as calcinations, sintering, and drying. Moreover, all these methods also require different solvents, polymerizing and chelating agents, *etc*. Hence, it is useful to develop effective low temperature synthesis methods to synthesize single phase and stoichiometric $BiFeO_3$. The present study explores and compares the possibilities of the low temperature synthesis of $BiFeO_3$ using different modifications in the conventionally used co-precipitation method. Highly basic environments involving rapid and complete precipitation of metal ions lead towards a lower synthesis temperature. Moreover, the study is also partially devoted to observing the thermal stability of the obtained $BiFeO_3$ with time and temperature, and the reversibility of $BiFeO_3$ after decomposition at higher temperatures.

EXPERIMENTAL

Synthesis

Bismuth ferrite crystallites were prepared by two different low temperature chemical solution methods: (a) the modified co-precipitation method (CPM1), as suggested by Ke et al.[19] but using KOH as precipitating agent instead of NH_4OH and b) the rich hydroxide co-precipitation method (CPM2) involving highly basic environment for rapid and complete precipitation. The starting precursors were iron nitrate $Fe(NO_3)_3{\cdot}9H_2O$ (99.99% pure), bismuth nitrate $Bi(NO_3)_3{\cdot}5H_2O$ (99.99% pure), potassium hydroxide KOH and nitric acid HNO_3. 0.2 M solution of $Fe(NO_3)_3{\cdot}9H_2O$ in 100 ml deionized water and 0.2 M solution of $Bi(NO_3)_3{\cdot}5H_2O$ in 100 ml dilute nitric acid were prepared. These solutions were mixed and stirred for 30 min with the help of a magnetic stirrer, and the resulting solution was named as a metal ions solution.

In order to achieve the homogeneous precipitation of the metal ions in the CPM1 method, the metal ions solution was slowly added drop-wise to 400 ml of 1 M KOH aqueous solution. Because the homogenous precipitation is dependent upon the pH of the solution, an additional 200 ml of 2.2 M KOH solution was prepared and slowly added drop-wise to the metal nitrates solutions. In the CPM2 method, in contrast to the CPM1 method of,[19] the highly basic solution of 4 M KOH (400 ml) was first used. Secondly, this solution was added rapidly with vigorous stirring instead of drop-wise addition in the metal ions solution. The stirring continued for about 20–25 min.

The collected precipitates from the CPM1 and CPM2 methods were washed repeatedly with deionized water. The precipitates were then filtered and dried in a microwave oven. In the end, these powders were ground for 1 h with the help of a mortar and pestle.

Characterization

All obtained powders from grinding the dried precipitates were subjected to thermal analysis (TG/DSC). The TG/DSC model Q600 is equipped with a gas purging of nitrogen and platinum crucibles. Data was collected with a heating rate of 10°C/min to investigate the thermal behavior of the powder. In order to investigate the effects of heat treatment temperature and time on the crystallographic phase formation, the heat treated powders were subjected to an x-ray diffraction (XRD) experiment. The XRD patterns were collected using Philip's PANalytical X'Pert XRD system with CuKα radiations (λ = 1.5410 Å). The data were recorded by step scanning in the angular range (2θ) between 20° and 80° at a step size of 0.02° and a counting time of 2 s/step. The powder obtained from the CPM2 method was subjected to a field emission scanning electron microscope (FESEM), model Nova NanoSEM 450, to investigate morphology and particle size. ^{57}Fe Mössbauer spectra of the powder obtained from CPM2 was collected at room temperature in transmission mode. ^{57}Co in a Rh matrix was used as the source. Data analysis was performed using a MOS-90 computer program,[28] assuming that all the peaks were Lorentzian in shape. The Mössbauer spectrometer was calibrated using a thin α-Fe foil. The field dependence of the magnetization (MH curve) at room temperature was explored using a vibrating sample magnetometer (VSM). The magnetic hysteresis loop was measured in a field sweep from −2 to 2 Tesla.

RESULTS AND DISCUSSION

Co-precipitation Method: (CPM1)

Figure 1 shows the TG/DSC curves of dry precipitate obtained from the CPM1 method. The TG curve shows weight loss of about 10.5% at up to 450°C. This weight loss can be due to the evaporation of residual water and decomposition of hydroxides. Above this temperature, weight loss is negligible until 600°C. The DSC curve shows associated broad exothermic peaks centered at about 270°C and 470°C. However, upon magnification, the DSC curve shows another broader exothermic peak at 550°C, which is shown in the inset of Fig. 1. In order to investigate the changes incorporated by these peaks on the crystallinity, the precipitates were selectively heat treated at 250°C, 500°C, 550°C, and 650°C for 4 h at each temperature.

Figure 2 shows the XRD patterns collected at room temperature for these treated powders. The XRD pattern collected for the powder treated at 250°C is characteristic for the crystalline phases

Table I. The comparison of the existing BFO synthesis methods

Method	Secondary phases during synthesis	Special equipment needed	Parameters to be controlled (treatment temperature and time common of all)	Calcination temperature	Refs.
Solid state	$Bi_{25}FeO_{40}$, $Bi_2Fe_{2.75}$, $Bi_2Fe_4O_9$, Bi_2O_3 and Fe_2O_3	Ball Mill (ethanol as liquid medium)[8,9]	Milling speed and time	> 600°C	Refs. 8 and 10
Hydrothermal	$Bi_2Fe_4O_9$, $Bi_{25}FeO_{40}$ and $Bi_{12}(Bi_{0.5}\text{-}Fe_{0.5})O_{19.5}$	Auto-clave	Concentration of Mineralizers such as KOH and NaOH,	Approximately 200–240°C (low yield)	Refs. 11–13
Microwave Hydrothermal	$Bi_2Fe_4O_9$, $Bi_{25}FeO_{39}$, $Bi(OH)_3$, Bi_2O_3 and Fe_2O_3	Autoclave, microwave furnace and centrifugation machine	Concentration of Mineralizers such as KOH and NaOH	Approximately 180°C (low yield)	Refs. 14 and 15
Sol–gel	$Bi_2(CO_3)O_2$, Bi_2O_3 and Fe_2O_3		Concentration of chelating agent such as citric acid	450–650°C	Refs. 16 and 17
Conventional co-precipitation	Bi_2O_3 and $Bi_2Fe_4O_9$		Concentration of precipitating agent such as KOH and NH_4OH	600°C	Ref. 18
Modified co-precipitation (as suggested by Ke et al.[19]	Bi_2O_3, $Bi_2Fe_4O_9$ and $Bi_{25}FeO_{39}$		Concentration of precipitating agent such NH_4OH and ratio of Bi content	550°C only when Bi content is 3% excess	Ref. 19
Rapid liquid sintering	$Bi_{25}FeO_{39}$ and $Bi_{36}\text{-}Fe_2O_{57}$	Rapid thermal annealing system		880–910°C	Refs. 20 and 21
Metal complex powders	$Bi_{25}FeO_{40}$, $Bi_2Fe_4O_9$ and Bi_2O_3		Concentration of chelating agents such as citric acid, EDTA and tartaric acid	600°C	Refs. 22 and 23
Modified Pechini method	$Bi_2Fe_4O_9$, $Bi_{25}FeO_{40}$ and $Bi_{36}Fe_2O_{57}$		Concentration of chelating agents (citric acid and tartaric acid) and polymerizing agents such as ethylene glycol	600°C	Refs. 24–26
Hydro-Evaporation	$Bi_{25}FeO_{40}$			650°C	Ref. 27
CPM1	Bi_2O_3		Concentration of precipitating agent	550°C	Current study
CPM2			Concentration of precipitating agent	400°C	Current study

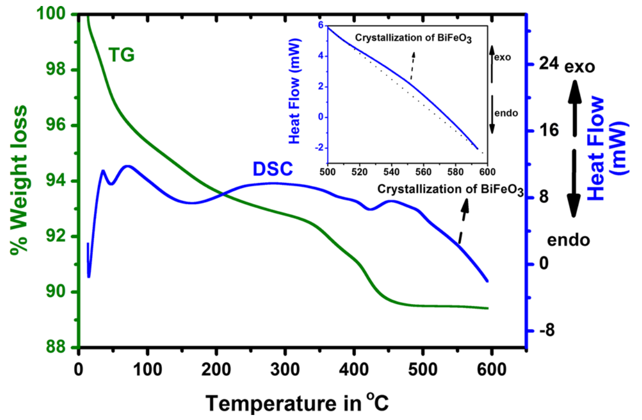

Fig. 1. TG/DSC curves for the dry precipitate obtained from the CPM1 method. Inset is the magnification of Fig. 5 in the shown temperature range.

along with signs of the amorphous phase. On analysis of the XRD pattern after treatment at 500°C, the amorphous phase is found to transfer into the crystalline phase. It is believed that heating the precipitates, which actually are amorphous Bi and Fe hydroxides, progressively decomposes and transforms them to the crystalline phase. This assumption can get confidence from the progressive weight loss in Fig. 1 at up to 450°C on heating the precipitates. The effects of further increase in the treatment temperature to 550°C indicate the formation of $BiFeO_3$ with a small impurity peak characteristic of Bi_2O_3 at about 2θ of 28°. The successive disappearance of the impurity peak with the increase in heat treatment time at 550°C in Fig. 3 indicates that this impurity is not due to the decomposition of $BiFeO_3$. If the decomposition of $BiFeO_3$ at this temperature has been involved, then the increase in treatment time was expected to increase the intensity of the associated peak.

Increase in the heat treatment temperature to 650°C causes appearance of new peaks at 2θ values of 27.5°, 28°, and 33° characteristics of °sillenite $Bi_{25}FeO_{39}$, bismuth oxide Bi_2O_3 and Fe_2O_3, respectively, indicating the decomposition of $BiFeO_3$. This result is consistent with the previous reports claiming the narrow stability range for $BiFeO_3$.[29,30] In order to check the reversibility of the decomposition, the powder treated at 650°C was heated again at 550°C for 4 h, whose XRD pattern is also shown in Fig. 2. It was found that the decomposition of $BiFeO_3$ is irreversible. Once decomposed, it becomes very hard to form $BiFeO_3$ again.

Co-precipitation Method: (CPM2)

Figure 4 shows the TG/DSC curves for the dry precipitate obtained from the CPM2 method. The weight loss in the TG curve can be divided into two regions, above and below 400°C. The weight loss of about 8% at up to 400°C can be expected due to the residual water evaporation and decomposition of hydrates. The second region above 400°C comprises a weight loss of 3.5%. In order to investigate the origin behind these weight losses, the dry precipitates were heat treated at 400°C and 550°C for 4 h.

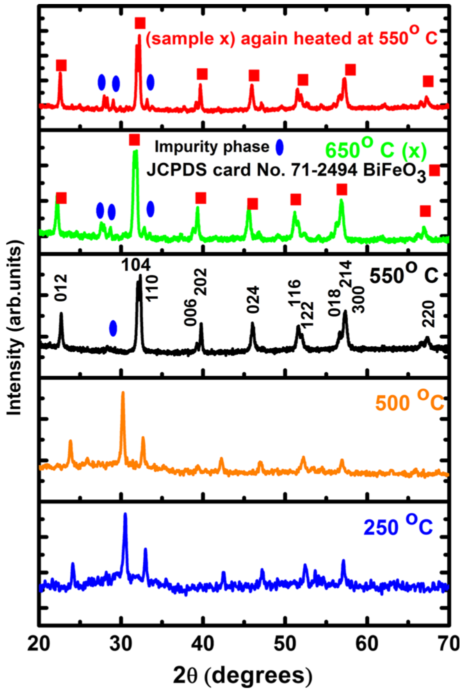

Fig. 2. XRD patterns collected at room temperature for the powder treated at 250°C, 500°C, 550°C, 650°C, and 650°C powder again at 550°C for 4 h, respectively, in the CPM1 method.

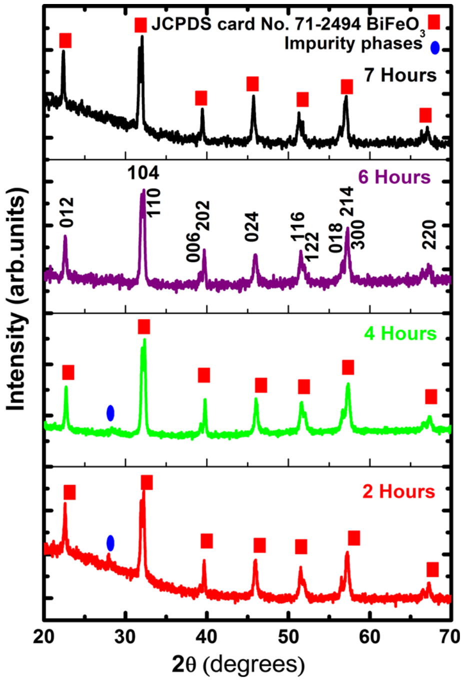

Fig. 3. XRD patterns collected at room temperature for the powder treated at 550°C for 2 h, 4 h, 6 h, and 7 h, respectively, in the CPM1 method.

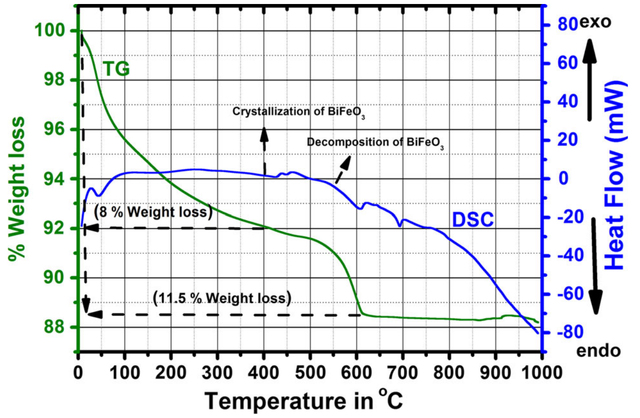

Fig. 4. TG/DSC curves for the dry precipitates obtained from the CPM2 method. The crystallization and decomposition temperature are highlighted with the help of results of XRD in Fig. 5.

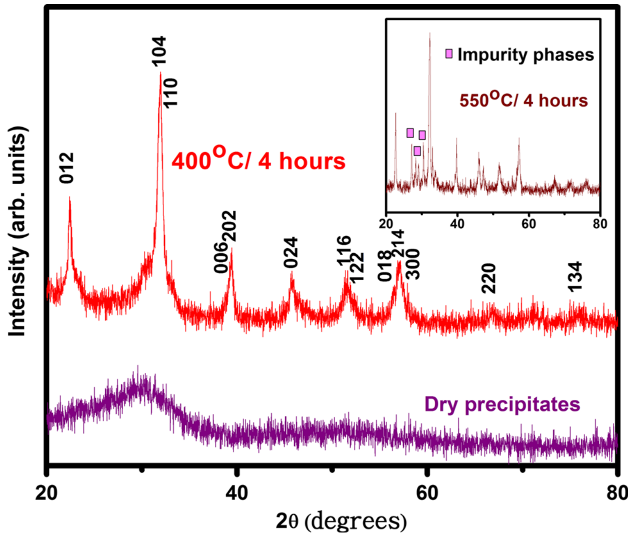

Fig. 5. XRD patterns collected at room temperature for the precipitates and powder treated at 400°C and 550°C for 4 h, respectively, in the CPM2 method.

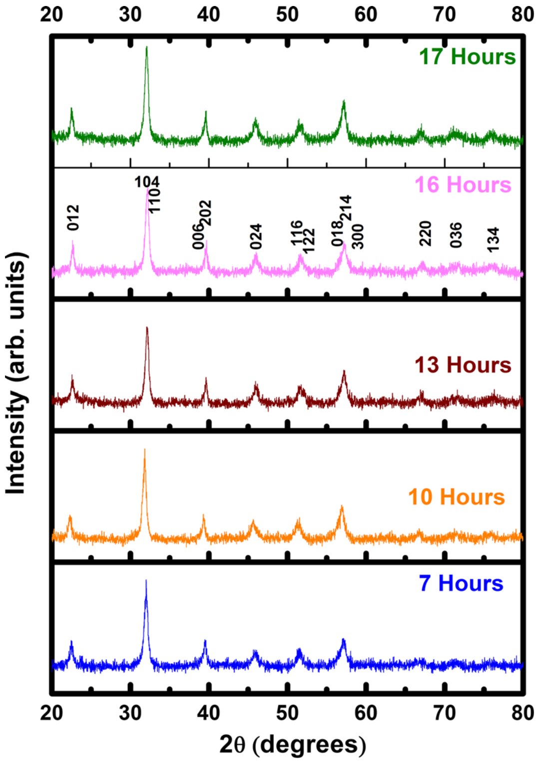

Fig. 6. XRD patterns collected at room temperature for the powder treated at 400°C up to 19 h in the CPM2 method.

XRD patterns in Fig. 5 show that the dry precipitates are amorphous. The reflection peaks appeared, all characteristics of rhombohedral $BiFeO_3$ (JCPDS card No. 71-2494, space group R3c) for the sample treated at 400°C for 4 h. However, iron oxide Fe_2O_3 and sillenite $Bi_{25}FeO_{39}$ (impurity phases) were present in the $BiFeO_3$ phase for the sample heat treated at 550°C for 4 h. So, it is concluded that weight loss below 400°C is due to the decomposition of hydrates and evaporation of residual water and at above 400°C, weight loss is due to decomposition of $BiFeO_3$. Figure 6 shows high stability of $BiFeO_3$ at 400°C. The absence of any impurity peaks on heating the sample up to 19 h suggested $BiFeO_3$ is thermally stable at 400°C.

On the basis of these results, it can be confirmed that the CPM2 method is easy, simple, impurity-free, and the synthesis temperature is lower when compared to other methods listed in Table I. The only hydrothermal method requires relatively lower synthesis temperature. On the other hand, hydrothermal methods have comparatively lower yield and harder control of synthesis parameters, such as pressure, PH, microwave intensity, treatment temperature, and treatment time. Rich hydroxide (OH^{-1}) environment in the CPM2 methods might have been suitable for the complete precipitation of metal ions. Otherwise, without complete precipitation, the ratio of Bi/Fe (1:1) will be disturbed in precipitates and will result in impurity phases.[11] Because the study was triggered by the motivation to synthesize and characterize $BiFeO_3$ at low temperatures, henceforth the current article will focus on $BiFeO_3$ obtained by the CPM2 method because of its low synthesis temperature.

FESEM

Figure 7 shows the FESEM image of $BiFeO_3$ obtained from the CPM2 method and its particle size distribution. The average particle size was about 50–60 nm. The particle size distribution shows that the size of about 68% of the particles is between 35 nm and 95 nm, whereas about 12% of the particles are below 35 nm, and about 20% of the particles are above 95 nm in size.

Mössbauer Spectroscopy

Figure 8 shows the room temperature ^{57}Fe Mössbauer spectrum powder obtained from the CPM2

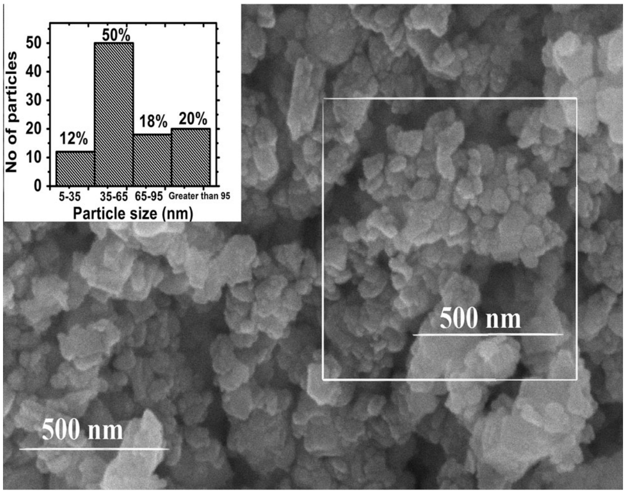

Fig. 7. FESEM image of $BiFeO_3$ obtained from CPM2 method. Inset shows particle size distribution of region highlighted in Fig. 7.

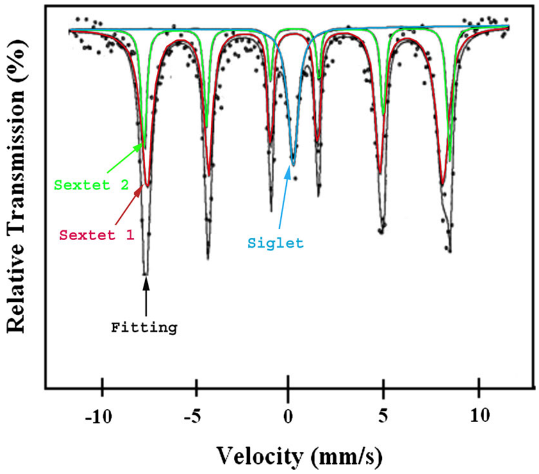

Fig. 8. Room temperature Fe^{57} Mössbauer spectra of $BiFeO_3$ obtained from the CPM2 method.

method. The spectrum shown is best fitted by the appearance of two sextets and a singlet structure. The sextets comprise isomer shifts of $\delta = 0.44$ mm/s and 0.36 mm/s, with associated hyperfine fields of $H_{\mathrm{eff}} = 508$ kOe and 492 kOe, and 23% and 65% of the spectral area respectively. The singlet comprises an isomer shift of 0.31 mm/s, with an associated 12% spectral area. It is well known that the oxidation state of octahedrally coordinated Fe should be mainly distinguished by an isomer shift, 0.6–1.7 mm/s typical for Fe^{2+}, 0.05–0.5 mm/s typical for Fe^{3+} and -0.15 mm/s to 0.05 mm/s typical for Fe^{4+} (relative to the a-Fe standard). These observed values of isomer shifts for both the sextets and singlet are typical for the high spin Fe^{+3} in octahedral oxygen coordination,[31] indicating that the prepared $BiFeO_3$ is free from oxygen vacancies. The absence of oxygen evaporation might have been possible by the low temperature at 400°C involved in the CPM2 method. Stoichiometric oxygen and absence of multiple oxidation states of Fe are desired for the reduction of leakage current, which limits the practical application of $BiFeO_3$.[32] Lorenz et al.[33] reported that magneto-electric coupling is higher for low density of oxygen related defects. Hence, the $BiFeO_3$ prepared by CPM2 can be useful for magneto-electric applications.

Before association of the ^{57}Fe Mössbauer features with the microstructure effects, a few findings from the literature are reviewed in the following text. Firstly, the magnetic structure of $BiFeO_3$ is a G-type antiferromagnetic. Also, the spin–orbit and exchange interactions produce spin canting which result in a spiral spin arrangement with a wavelength of about 62 nm.[34,35] Secondly, $BiFeO_3$ with particle size greater than spiral length are antiferromagnetic, exhibits only non-linear magneto-electric effect, and the volume average of linear magneto-electric effect is negligible.[36] However, suppression of spiral spin structure can produce weak ferromagnetism and giant linear magneto-electric effects.[37,38] Suppression of spin modulated structure can be introduced by using chemical doping,[39,40] applying a high magnetic field,[41–44] and reducing the particle size to less than spiral length.[45] Thirdly, Zhong et al.[46] suggested that the ferromagnetic response in $BiFeO_3$ is induced due to the destruction of cycloid spin structures in $BiFeO_3$. Therefore, the presence of ferromagnetic behavior is an indication of suppression of the cycloid spin structure. Many reports are available showing that spiral spin structures collapse below 62 nm.[34,35,45] However, few articles report the appearance of ferromagnetic responses even at less than 95 nm[47] and less than 83 nm.[48] However, on the basis of very limited literature on this issue, it is very hard to conclude about the exact size of particles below which the suppression starts. At this stage, following experiment results of Park et al.[47] a distribution of particles below and above 95 nm is shown in the inset of Fig. 7. Moreover, it is also reported that the hyperfine field associated with the magnetic sextet in the Mössbauer spectrum is higher for larger particles.[47,49]

On basis of the above discussion, the currently observed sextet comprising 23% of the spectral area and the associated relatively higher hyperfine field of 508 kOe can be attributed to the antiferromagnetic effects arising from particles greater than 95 nm with a spiral spin structure. The second sextet with 65% spectral area and the associated relatively smaller hyperfine field of 492 kOe is an average weak ferromagnetic response from the wide particle size distribution below 95 nm with a suppressed spiral spin. Park[47] and Castillo et al.[50] indicated the presence of superparamagnetic phase in less than 50 nm $BiFeO_3$ nanoparticles. Therefore, the appearance of singlet structure can be attributed to the superparamagnetic effects arising from smaller particles in the sample.[47,50]

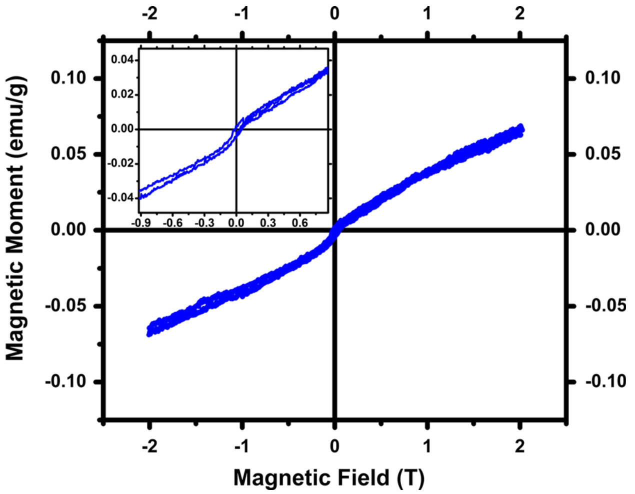

Fig. 9. Room temperature field dependence of magnetization of $BiFeO_3$ obtained from the CPM2 method. Inset shows the same hysteresis loop in the low field region.

Sextet 1 comprising 23% spectral area can be attributed only to non-linear magneto-electric effects. The ferromagnetic response is a result of suppression in the cycloidal spin arrangements and is also coupled by a giant increase in the linear magneto-electric coefficient. Therefore, the second sextet comprising 65% of spectral area is of greater importance and can enhance the linear magneto-electric coupling drastically.

Field Dependent Magnetization

Figure 9 shows the MH curve traced at room temperature for $BiFeO_3$ nanoparticles prepared by the CPM2 method. The MH curve shows hysteresis behavior with an unsaturated tail up to 2 Tesla, the maximum value of the applied magnetic field. The observed MH curve can be conferred in the terms of superposition of a ferromagnetic loop on an unsaturated antiferromagnetic tail. The coercive field value measured from the hysteresis loop is about 3 kOe, which can also be seen in the inset of Fig. 9. Bulk $BiFeO_3$ is an antiferromagnetic system,[16] however, a weak ferromagnetic response can be observed for smaller particles with suppressed spiral spin structures.[46–48] The presence of antiferromagnetic and weak ferromagnetic behavior can be conferred on the basis of particle size distribution and the presence of two sextets in the Mössbauer spectra. The larger particles in the prepared sample with the spiral spin structure show antiferromagnetic behavior as sextet 1 in the Mössbauer spectra. However, the smaller particles with suppressed spiral spin structures can induce weak ferromagnetic responses as sextet 2 in the Mössbauer spectra.

The observed value of magnetization at 2 Tesla is relatively smaller,[14,45,48,51,52] whereas the coercive is relatively higher[14,45,48,51,52] when compared to $BiFeO_3$ nanoparticles prepared by other methods. The higher value of the magnetization of $BiFeO_3$ in[14,45,48,51,52] can arise due to the presence of ferromagnetic/ferrimagnetic impurities such as Fe_2O_3, Fe_3O_4, $Bi_2Fe_4O_9$. Moreover, the oxygen nonstoichiometry of $BiFeO_3$ prepared by other methods can give rise to multiple oxidation states of Fe, giving birth to incomplete spin cancellations in the spiral arrangements.[32,52] The higher coercive force can be attributed to the higher magneto-crystalline anisotropy arising from wide particle distributions in the present study.[45]

CONCLUSIONS

In short, the CPM2 method yields single phases of $BiFeO_3$ at 400°C in a very simple way. FESEM shows a wide particle size distribution with an average particle size of 50–60 nm. The observing of only trivalent states of iron in octahedral oxygen coordination has been conferred in terms of the absence of oxygen and bismuth evaporation owing to low synthesis temperature. The absence of oxygen vacancies and suppressed spiral spin structures in prepared $BiFeO_3$ not only minimizes the leakage current but also enhances the magneto-electric properties drastically.

ACKNOWLEDGEMENTS

The authors strongly acknowledge the Higher Education Commission of Pakistan for financial support under the startup research grant entitled “Synthesis and Electrical Characterization of $BiFeO_3$”. The authors also acknowledge the XRD facility at the Chemical Engineering Department, COMSATS Institute of Information and Technology, Defense Road, Off Raiwind Road, Lahore.

REFERENCES

1. W. Eerenstein, N.D. Mathur, and J.F. Scott, *Nature* 442, 759 (2006).
2. J.F. Scott and C.A.P. De Araujo, *Science* 246, 1400 (1989).
3. Z. Shi, C. Wang, X. Liu, and C. Nan, *Chin. Sci. Bull.* 53, 2135 (2008).
4. F. Yang, Y.C. Zhou, M.H. Tang, F. Liu, Y. Ma, X.J. Zheng, W.F. Zhao, H.Y. Xu, and Z.H. Sun, *J. Phys. D Appl. Phys.* 42, 72004 (2009).
5. J.-R. Cheng, N. Li, and L.E. Cross, *J. Appl. Phys.* 94, 5153 (2003).
6. T. Kimura, T. Goto, H. Shintani, K. Ishizaka, T. Arima, and Y. Tokura, *Nature* 426, 55 (2003).
7. K. Takahashi, N. Kida, and M. Tonouchi, *Phys. Rev. Lett.* 96, 117402 (2006).
8. P. Suresh and S. Srinath, *J. Alloys Compd.* 649, 843 (2015).
9. M. Bernardo, T. Jardiel, M. Peiteado, A. Caballero, and M. Villegas, *J. Eur. Ceram. Soc.* 31, 3047 (2011).
10. M.M. Kumar, V.R. Palkar, K. Srinivas, and S.V. Suryanarayana, *Appl. Phys. Lett.* 76, 2764 (2000).
11. D. Cai, J. Li, T. Tong, D. Jin, S. Yu, and J. Cheng, *Mater. Chem. Phys.* 134, 139 (2012).
12. A. Chaudhuri, S. Mitra, M. Mandal, and K. Mandal, *J. Alloys Compd.* 491, 703 (2010).
13. C. Chen, J. Cheng, S. Yu, L. Che, and Z. Meng, *J. Cryst. Growth* 291, 135 (2006).

14. Z. Wang, J. Zhu, W. Xu, J. Sui, H. Peng, and X. Tang, *Mater. Chem. Phys.* 135, 330 (2012).
15. G. Biasotto, A.Z. Simões, C. Foschini, M. Zaghete, J.A. Varela, and E. Longo, *Mater. Res. Bull.* 46, 2543 (2011).
16. J. Wei and D. Xue, *Mater. Res. Bull.* 43, 3368 (2008).
17. J.-H. Xu, H. Ke, D.-C. Jia, W. Wang, and Y. Zhou, *J. Alloys Compd.* 472, 473 (2009).
18. M.Y. Shami, M. Awan, and M. Anis-ur-Rehman, *J. Alloys Compd.* 509, 10139 (2011).
19. H. Ke, W. Wang, Y. Wang, J. Xu, D. Jia, Z. Lu, and Y. Zhou, *J. Alloys Compd.* 509, 2192 (2011).
20. Y. Wang, L. Zhou, M. Zhang, X. Chen, J. Liu, and Z. Liu, *Appl. Phys. Lett.* 84, 1731 (2004).
21. A. Sagdeo, P. Mondal, A. Upadhyay, A. Sinha, A. Srivastava, S. Gupta, P. Chowdhury, T. Ganguli, and S. Deb, *Solid State Sci.* 18, 1 (2013).
22. S. Ghosh, S. Dasgupta, A. Sen, and H.S. Maiti, *Mater. Res. Bull.* 40, 2073 (2005).
23. S. Ghosh, S. Dasgupta, A. Sen, and H.S. Maiti, *J. Am. Ceram. Soc.* 88, 1349 (2005).
24. S.M. Selbach, M.-A. Einarsrud, T. Tybell, and T. Grande, *J. Am. Ceram. Soc.* 90, 3430 (2007).
25. M. Popa, D. Crespo, and J.M. Calderon-Moreno, *J. Am. Ceram. Soc.* 90, 2723 (2007).
26. M. Kumar, K.L. Yadav, and G.D. Varma, *Mater. Lett.* 62, 1159 (2008).
27. M. Sakar, S. Balakumar, P. Saravanan, and S. Jaisankar, *Mater. Res. Bull.* 48, 2878 (2013).
28. G. Grobe, Version: *Mos-90: Manual and Program Documentation* (1992).
29. S.K. Korchagina, S.A. Ivanov, V.Y. Proidakova, S.N. Rush, and L.F. Rybakova, *Inorg. Mater.* 45, 568 (2009).
30. K. Nalwa, A. Garg, and A. Upadhayaya, *Indian J. Eng. Mater. Sci.* 15, 91 (2008).
31. N.N. Greenwood and T.C. Gibb, *Mössbauer Spectroscopy* (London: Chapman and Hall, 1971).
32. L.Y. Hui, S.G. Lin, C.F. Gao, and W.Z. Kui, *Chin. Phys. B* 19, 77702 (2010).
33. M. Lorenz, G. Wagner, V. Lazenka, P. Schwinkendorf, H. Modarresi, M.J.V. Bael, A. Vantomme, K. Temst, O. Oeckler, and M. Grundmann, *Appl. Phys. Lett.* 106, 12905 (2015).
34. I. Sosnowska, T.P. Neumaier, and E. Steichele, *J. Phys. C Solid State Phys.* 15, 4835 (1982).
35. I. Sosnowska and A. Zvezdin, *J. Magn. Magn. Mater.* 140, 167 (1995).
36. C.T. Munoz, J.P. Rivera, A. Bezinges, A. Monnier, and H. Schmid, *Jpn. J. Appl. Phys.* 24, 1051 (1985).
37. J. Wang, J.B. Neaton, H. Zheng, V. Nagarajan, S.B. Ogale, B. Liu, D. Viehland, V. Vaithyanathan, D.G. Schlom, U.V. Waghmare, N.A. Spaldin, K.M. Rabe, M. Wuttig, and R. Ramesh, *Science* 299, 1719 (2003).
38. A.F. Popkov, M.D. Davydova, K.A. Zvezdin, S.V. Solov'yov, and A.K. Zvezdin, *Phys. Rev. B* 93, 94435 (2016).
39. G. Le Bras, D. Colson, A. Forget, N. Genand-Riondet, R. Tourbot, and P. Bonville, *Phys. Rev. B* 80, 134417 (2009).
40. Z. Gabbasova, M. Kuz'min, A. Zvezdin, I. Dubenko, V. Murashov, D. Rakov, and I. Krynetsky, *Phys. Lett. A* 158, 491 (1991).
41. Y.F. Popov, A.K. Zvezdin, G.P. Vorob'ev, A.M. Kadomtseva, V.A. Murashev, and D.N. Rakov, *JETP Lett.* 57, 69 (1993).
42. Y.F. Popov, A.M. Kadomtseva, G.P. Vorob'ev, and A.K. Zvezdin, *Ferroelectrics* 162, 135 (1994).
43. Y.F. Popov, A.M. Kadomtseva, S.S. Krotov, D.V. Belov, G.P. Vorobev, P.N. Makhov, and A.K. Zvezdin, *Low Temp. Phys.* 27, 478 (2001).
44. B. Ruette, S. Zvyagin, A.P. Pyatakov, A. Bush, J.F. Li, V.I. Belotelov, A.K. Zvezdin, and D. Viehland, *Phys. Rev. B* 69, 64114 (2004).
45. S. Layek and H. Verma, *Adv. Mater. Lett.* 3, 533 (2012).
46. J. Zhong, J.J. Heremans, D. Viehland, G.T. Yee, and S. Priya, *Ferroelectrics* 400, 3 (2010).
47. T.-J. Park, G.C. Papaefthymiou, A.J. Viescas, A.R. Moodenbaugh, and S.S. Wong, *Nano Lett.* 7, 766 (2007).
48. F. Huang, Z. Wang, X. Lu, J. Zhang, K. Min, W. Lin, R. Ti, T.T. Xu, J. He, C. Yue, and J. Zhu, *Sci. rep.* 3, 2907 (2013).
49. R.K. Sharma, O. Suwalka, N. Lakshmi, and K. Venugopalan, *Synth. React. Inorg. Met. Org. Chem.* 36, 175 (2006).
50. M.E. Castillo, V. Shvartsman, D. Gobeljic, Y. Gao, J. Landers, H. Wende, and D. Lupascu, *Nanotechnology* 24, 355701 (2013).
51. A. Manzoor, S.K. Hasanain, A. Mumtaz, M.F. Bertino, and L. Franzel, *J. Nanopart. Res.* 14, 1310 (2012).
52. S. Hussain, S.K. Hasanain, G.H. Jaffari, N.Z. Ali, M. Siddique, and S.I. Shah, *J. Alloys Compd.* 622, 8 (2015).